

## Article

# Development of a Molecular Dynamics Model to Assess the Possibility of Type II/III Porous Liquid Formation

Hamed Faramarzi <sup>1</sup>, Masoud Rahimi <sup>1,\*</sup>, Hamidreza Mahdavi <sup>2,\*</sup> and Saber Niazi <sup>3</sup><sup>1</sup> Chemical Engineering Department, Razi University, Kermanshah 6714414971, Iran; hamed.181223@gmail.com<sup>2</sup> Department of Chemical and Biological Engineering, Monash University, Clayton, VIC 3800, Australia<sup>3</sup> Department of Mechanical, Chemical and Industrial Design Engineering, ETSIDI, Universidad Politécnica de Madrid (UPM), Ronda de Valencia 3, 28012 Madrid, Spain; s.niazi@upm.es

\* Correspondence: m.rahimi@razi.ac.ir (M.R.); hamidreza.mahdavi1@monash.edu (H.M.)

**Abstract:** The study of porous liquids (PLs) using molecular dynamics (MD) simulation is one of the most interesting and attractive research topics. The possibility of creating permanent porosity in a solvent and increasing its adsorption capacity is very practical. The purpose of the present study is to examine how an MD model can be developed to evaluate the possibility of PL formation. Additionally, the validation of the model was conducted by simulations using two metal–organic frameworks (MOFs) including zeolitic imidazolate framework-8 (ZIF-8) and Hong Kong University of Science and Technology-1 (HKUST-1) as porogens and water (H<sub>2</sub>O) and triethylene glycol (TEG) as solvents. The results revealed that H<sub>2</sub>O and TEG are incapable of penetrating the ZIF-8 pores due to their small size and unfavorable thermodynamics; however, both solvents easily penetrate through the large HKUST-1 pores. These observations aligned with findings from experimental literature studies, thus confirming the validity of the model. In order to expand the model's scope, the developed model was used to assess the possibility of PL formation using ZIF-8 and HKUST-1 with different pore and window sizes and shapes, and a wide range of hydrocarbon liquids with different molecular sizes and shapes as solvents. It was found that ZIF-8 can form PLs with a more extensive range of sterically hindered solvents due to its smaller apertures and incompatible shape. In addition, only a few solvents (e.g., n-pentane, benzene, 1,3,5-trimethylbenzene, 1,3,5-triisopropylcyclohexane, and 1,3,5-triisopropylbenzene) can partially penetrate its ZIF-8 pores without steric hindrance. These privileged solvents typically have an aspect ratio far from 1, indicating a more elongated shape, and/or more linear branches. In contrast, HKUST-1, which has larger apertures and a compatible shape, allows for complete penetration of specific solvents (e.g., benzene, iso-octane, n-pentane), thereby preventing PL formation with such combinations. In addition, cyclohexane has the ability to partially penetrate the pores of HKUST-1. Therefore, in addition to the size of the solvent molecule, one of the most important properties for penetration is the compatibility of the shape of the porogen pore window with the shape of the solvent molecule. This research provides important new information on how PLs come to be by illuminating the role that solvent molecules and porogen play in promoting penetration and, in the end, impacting the process of PL formation.

**Keywords:** porous liquid; permeant porosity; molecular dynamics simulation; solvent size and shape; porogen window size and shape



**Citation:** Faramarzi, H.; Rahimi, M.; Mahdavi, H.; Niazi, S. Development of a Molecular Dynamics Model to Assess the Possibility of Type II/III Porous Liquid Formation. *Processes* **2024**, *12*, 762. <https://doi.org/10.3390/pr12040762>

Academic Editor: Andrew S. Paluch

Received: 8 March 2024

Revised: 3 April 2024

Accepted: 8 April 2024

Published: 10 April 2024



**Copyright:** © 2024 by the authors. Licensee MDPI, Basel, Switzerland. This article is an open access article distributed under the terms and conditions of the Creative Commons Attribution (CC BY) license (<https://creativecommons.org/licenses/by/4.0/>).

## 1. Introduction

Sorption refers to the interaction between an adsorbate and an adsorbent, such as a liquid or solid, intending to separate a mixture [1]. Liquid sorbents demonstrate high absorption capacity and selectivity, fast kinetics, and suitability for application in continuous cycle processes [2–4]. Nevertheless, they have elevated energy demands for the release of sorbents and the regeneration of liquids owing to chemical interactions, as well as additional concerns such as volatility and corrosiveness [5]. On the other hand, porous solids

often have a high adsorption capacity and low-energy adsorption, can act as molecular sieves, and display excellent selectivity due to their large surface area resulting from persistent porosity [2,6,7]. However, they also have challenges in optimizing exposed surface areas, separating particulate material, and dealing with operational complexity, as well as unfavorable thermodynamics, and high capital demands [3,8]. These positives and negatives gave rise to the concept of porous liquids (PLs), which is the production of a liquid that, in addition to its fluidity, also benefits from the porosity of solids [2,9–11]. The concept of PLs was first introduced in 2007 by James et al. [12]. It was believed that PLs could exist if the molecules of the liquid had permanent empty pores or extrinsic porosity [3,9]. Although molecules in liquids form microscopic spaces between one another, these spaces are confined to transient and intrinsic porosities [13–16]. Therefore, PL formation relies on the creation of permanent spaces of well-defined size inside the molecules of liquids [17,18]. PLs fall into three categories: type I, type II, and type III [19,20]. Type I PLs consist of a single rigid molecule or compound containing both liquid and permanent porosity [9,21]. Type II PLs are formed when a porous solid (porogen) is dissolved in a solvent that is excluded from the pores [22,23]. Type III PLs are formed when porogens are dispersed in a solvent that is sterically incapable of occupying the pores [24,25]. In fact, type II and type III PLs are distinguished from one another by the degree to which the porogen is dissolved or merely dispersed in the solvent [26]. Regarding industrial applications, type II and III PLs hold the most promise [27].

A variety of porogens have been investigated to form type II and III PLs, including metal–organic frameworks (MOFs), zeolites, porous carbon, and silica nanoparticles [11,14,28,29]. Porogens are prioritized whenever the size of their window is large enough to allow guest species penetration but too small for solvent penetration [30]. In addition, they are prioritized whenever the shape of the porogens window is incompatible with the shape of the solvent [23,31]. Rigid porogens that have restricted access windows help to eliminate the possibility of the pores becoming accidentally occupied (i.e., the pores can be kept empty and accessible) [32]. Solvents with larger molecular sizes are preferred, as their substantial size typically restricts penetration. Furthermore, they are more preferred when the geometry of the solvent's shape is incompatible with the window structure of the porogen. Therefore, solvent shapes (geometries including linear, branching, spherical, triangular, rectangular, rod, and disk), in addition to their molecular dimension sizes (including width, height, and depth), must be carefully considered [23,31]. Additionally, solvents with large molecular dimensions, such as an ionic liquid, a liquid polymer, or a deep eutectic solvent, are frequently utilized to reduce the likelihood of the solvent permeating porogens [25,33]. PLs of type II and III can be synthesized from a wide range of MOFs and solvents, resulting in nearly infinite variations [27].

Several solvent variables must be considered to create a stable PL with porosity and fluidity. Size, shape, physical qualities, and intermolecular interactions are crucial. Chemical and thermal stability, biocompatibility, low vapor pressure, low melting point, low specific heat, non-corrosiveness, and low viscosity and density should be considered. Finding a solvent that fits all of these characteristics is complex and time-consuming. Given the wide variety of porogens and solvents that can go into the formation of type II and III PLs, it is abundantly obvious that the full extent of these different formulations has not yet been investigated to their full potential [25,34]. However, characterizing the porosity of PLs remains a challenge due to the limitations of traditional methods for these unique materials. While established techniques like positron annihilation lifetime spectroscopy (PALS) exist, they are often inaccessible and require complex data analysis [26]. Additionally, PL production can be expensive due to the time and resources needed for experimental verification of their formation. Therefore, developing accessible and applicable characterization methods, such as computational screening techniques, is crucial. In this regard, molecular dynamics (MD) simulations offer a valuable tool. By considering the solvent and porogen characteristics such as shape and size, MD models can be developed to evaluate PL formation. The development of reliable models for assessing PL formation necessitates

a detailed understanding of these materials' properties at the nanoscopic level. MD simulations hold significant promise in providing the necessary characterization for this purpose, thereby accelerating advancements in the field of PLs. Despite the clear relevance of these theoretical approaches, the available literature on their application in PL research remains scarce [35,36]. MD is a computational technique that simulates the interplay between solvent and porogen characteristics such as shape and size. It is crucial to investigate, at an atomic level, how these characteristics affect the formation of PLs.

There has been a limited amount of research on MD simulations for investigating PLs in recent years. Melaugh et al. modeled hollow cage-like molecules functionalized with hydrocarbon chains to render them liquid at room temperatures using MD simulations. It was found that hydrocarbon chains can turn solids into liquid and modify PL characteristics, and that alkyl chains and their branching impact the melting temperature, fluidity, and porosity of type I PLs [37]. Later, Giri et al. studied type II PL formation using organic cages with a 5 Å central cavity, dissolved in 15-crown-5 and hexachloropropene (PCP) solvents through MD simulations. It was confirmed that these configurations formed PLs and notably enhanced methane gas solubility compared to non-porous solvents [3]. In 2016, Greenaway et al. performed a computational study of PLs using MD simulations. They monitored the diffusion of the PCP solvent in the organic cages named CC13. Their simulations showed that the PCP solvent is unable to diffuse into the cage cores of the PL, thus maintaining the intrinsic cage cavities and forming a type II PL [10]. Gomes et al. employed MD simulations to investigate the intricate molecular interactions and structural arrangements governing the formation and properties of type III PLs derived from dispersing MOFs (zeolitic imidazolate framework-8 (ZIF-8), Hong Kong university of science and technology-1 (HKUST-1), and Mg(II) metal-organic framework-74 (Mg-MOF-74)) in bis(trifluoromethylsulfonyl)azanide, trihexyl(tetradecyl)phosphonium ([P6,6,6,14][NTf<sub>2</sub>]) as an ionic liquid (IL) [38]. Sheng et al. conducted MD simulations that show the formation of type I PL using liquefied SiO<sub>2</sub> nanoparticles. They showed that interface interaction energies and van der Waals forces cause SiO<sub>2</sub> nanoparticles to aggregate, but modification reduces it. Higher nanoparticle grafting densities reduce aggregation and increase distance between nanoparticles, hence increasing the stability and fluidity of the resulting type I PL [39]. Furthermore, in another study, they used MD simulations to show that in SiO<sub>2</sub>-assisted type I PLs, steric repulsion and canopy-nanoparticle interactions influence stability and fluidity. Their findings suggest that controlling pore size is crucial for optimizing the stability and gas sorption capacity of PLs [40]. In 2021, Avila et al. conducted MD simulations to study the mechanisms of gas absorption in type III PLs (ZIF-8 and [P6,6,6,14][NTf<sub>2</sub>]). Simulations demonstrated that gas transfer from the IL to the MOF is energetic and structural, driven by gas affinity for the MOF's metallic centers. Gases affect liquid mass transport differently, hence their presence can influence PL transport properties [41]. Recently, Zhao et al. performed an MD simulation study that revealed that CO<sub>2</sub> diffusion in type III PLs is enhanced with increasing temperature and CO<sub>2</sub> loading, but it is insensitive to pressure [42].

Considering this body of research so far, a comprehensive and systematic MD model to assess type II/III PL formation which underscores the critical role of porogen and solvent characteristics is necessary. Therefore, the goal of this study is to examine how an MD model can be developed to evaluate the possibility of PL formation using porogens and solvents before experimental execution to provide an accessible and cost-effective approach. For this purpose, the MD model implemented mean square displacement (MSD), visual observations, and concentration profiles as primary tools. The strategic integration of the size and shape exclusion principle guided the study, emphasizing the effects of porogen size and shape, as well as solvent size, shape, and branches, on partial and complete penetration. The MD model not only enhances comprehension of the development of type II and III PL but also tackles complexities related to porogen properties and solvent selection, offering valuable insights to inform future experimental studies.

In this research, an MD model has been established, and the validation of the model was conducted by simulations using ZIF-8 and HKUST-1 as porogens and water (H<sub>2</sub>O) and triethylene glycol (TEG) as solvents. ZIF-8 and HKUST-1 were selected due to their distinct structural characteristics such as varying pores, window sizes, and also their prevalent use in PL research, especially in the formation of type II and III PLs. Additionally, the model was used to assess the possibility of PL formation using ZIF-8 and HKUST-1 with different pore and window sizes and shapes as porogens and hydrocarbon liquids with different molecular sizes and shapes solvents [43].

## 2. Modeling

The crystal structures of ZIF-8 and HKUST-1 simulated here are represented in Figure 1. According to the known mass-to-volume ratio, the number of solvent molecules was determined. In order to study the interactions between MOFs and solvents using computational modeling, a crucial initial step entails the cleavage of the MOF crystal structure along a specified plane. As a result, it is crucial to saturate the dangling bonds, which are present on the external surface of the MOF. The saturation is accomplished by coordinating the exposed open metal sites with the organic ligands and attaching hydrogen atoms or any other appropriate groups to electronegative atoms that do not have an enclosed valence electron shell. The main objectives are to ensure that the MOFs remain energetically stable, to inhibit the reactivity of active atoms with other molecules present in the system, and to enable realistic simulations. In the context of this research, hydrogen atoms were introduced to saturate the cleaved surfaces of HKUST-1, whereas 2-methyl imidazole groups were employed to fully occupy the cleaved surfaces of ZIF-8 [38,44]. Moreover, maintaining electro-neutrality inside the system was a crucial aspect in guaranteeing the accuracy of the MD simulations. Therefore, after the saturation of exposed bonds on crystal surfaces, careful consideration was made to preserve a total charge of zero by adjusting the number of counterions [45].

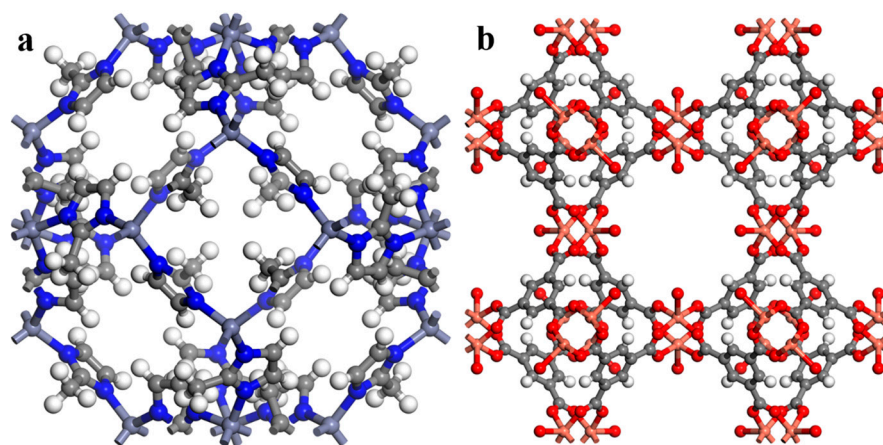


**Figure 1.** The structure of the porogens' unit cells, (a) ZIF-8 and (b) HKUST-1.

As shown in Figure 2, the simulation system was considered as a box containing two slab parts, made by placing one slab of MOF parallel to the xy plane and a slab of solvent with the same thickness (the number of solvent atoms depending on density). For ZIF-8, the z-coordinate range of the simulation box from 0 to 16.9 Å was assigned to the solvent, and the region from 16.9 to 33.8 Å was dedicated to the ZIF-8 framework. Similarly, due to the different sizes of HKUST-1, the solvent occupied the z-coordinate range from 0 to 26.3 Å, and the HKUST-1 framework resided in the region from 26.3 to 52.6 Å. The dimensions of the various MOF slabs are detailed in Table 1. The simulation boxes of ZIF-8 and HKUST-1 and their size can be seen in Figure 3. Forcite module of Materials Studio version 17.1.0.48. was employed for all simulations, utilizing the Universal Force Field (UFF) [46–48]. This force field is a more general-purpose force field that is

built on simple principles and atomic parameters and is capable of recreating the majority of the structural characteristics of the periodic table with errors of less than 0.1 Å in bond distances and 5 to 10° in angle bends [42,49]. Also, the selection of a rigid model framework for porogens in this study is supported by methodologies employed in similar fields of research. Insights into the adsorption and diffusion properties of gases in ZIF-8 have been provided by a study conducted by Paudel et al., where a rigid framework was utilized, demonstrating that substantial findings can be derived from such an approach [50]. Furthermore, the work of Zhao on the diffusion of CO<sub>2</sub> in type III PLs, employing the UFF forcefield [42]. Moreover, in the work of Zhao et al., it is observed that the effect of framework flexibility on CO<sub>2</sub> adsorption in HKUST-1 at 298 K is insignificant, with no discernible difference between the rigid and flexible models [51]. Therefore, the rigid model of UFF was chosen for this study. Following the approach of Rappe et al., we adjusted force field parameters where necessary (detailed in Table 2) [52]. However, for H<sub>2</sub>O, TEG, and other solvents, the original Lennard-Jones (LJ) potential parameters from the UFF forcefield were retained [42]. Geometry optimization employed the Smart algorithm with an energy convergence criterion of  $1 \times 10^{-2}$  kcal·mol<sup>-1</sup> and a maximum of  $1.5 \times 10^4$  iterations within the NVT ensemble. Subsequently, solvent density measurements were crucial to validate the force field. Achieving a low percentage error confirmed the suitability of the force field for simulations. Therefore, simulations of all pure solvents were performed at 293.15 K and 1 atm. To maintain constant pressure and temperature during these simulations, the NPT ensemble was employed with the Nose thermostat and Andersen barostat algorithm [39,53].

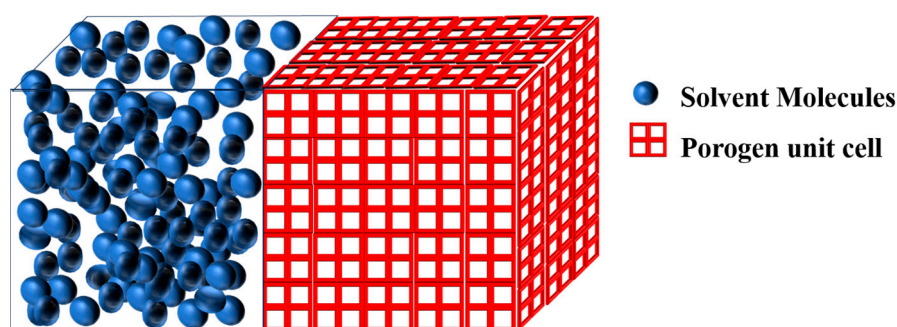


Figure 2. The general structure of the simulation box.

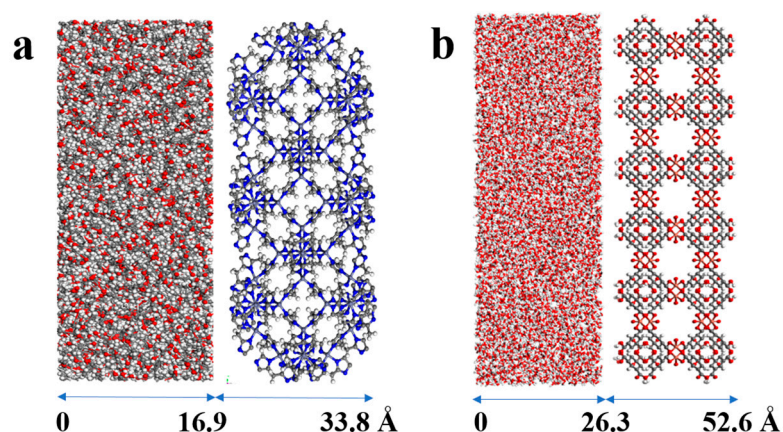


Figure 3. Simulation box of (a) ZIF-8-solvent and (b) HKUST-1-solvent combinations.

**Table 1.** The dimensions of MOF slabs were duplicated with periodic boundary conditions and used for MD simulation.

MOF	MOF Unit-Cell Replication	MOF Slab Dimensions (Å)
ZIF-8	3 3 1	50.8 × 50.8 × 16.9
HKUST-1	3 3 1	78.9 × 78.9 × 26.3

**Table 2.** Forcefield parameters for ZIF-8 and HKUST-1 [52].

Porous Solid	Atom	$\epsilon$ (kcal·mol <sup>-1</sup> )	$\sigma$ (Å)
ZIF-8	Zn	0.124	2.462
	N	0.069	3.261
	C1 (CNN)	0.105	3.431
	C2 (CNH)	0.105	3.431
	C3 (CHHH)	0.105	3.431
	H2 (-C2)	0.044	2.571
	H3 (-C3)	0.044	2.571
HKUST-1	Cu	0.005	3.114
	O	0.060	3.118
	C1 (COO)	0.105	3.431
	C2 (CCC)	0.105	3.431
	C3 (CCH)	0.105	3.431
	H	0.044	2.571

For the simulation of the main simulation box (which contains both porogen and solvent), first, the geometry optimization was done with the smart algorithm. Then, a preliminary simulation was done with the NVE ensemble with a time of 500 ps for the relaxation of the structure. Following the initial optimizations, the main simulations were conducted at a constant temperature of 293.15 K and pressure of 1 atm. A Nose thermostat was employed to ensure isothermal conditions throughout the simulation. The NVT ensemble, suited for studying molecular trajectories, was implemented with periodic boundary conditions. Electrostatic interactions were calculated using the Ewald summation method, while van der Waals forces were computed using an atom-based approach. The simulations ran for a total of 5 ns with a time step of 1 fs. System data were collected every 100 steps for further analysis [54,55]. The logic behind setting the simulation time at 5 ns was multiple: it was not only longer than the durations used in the studies cited [39,53–56], but it was also sufficient enough to assess the possibility of solvent molecules penetrating porogens within a reasonable simulation time.

In order to obtain a suitable model for assessing PL formation, first, it was necessary to validate it using benchmarks. Hence, the validation of the model was conducted by simulations using ZIF-8 and HKUST-1 as porogen and H<sub>2</sub>O and TEG as solvents. It is crucial to take into account the chemical stability of porogen in the presence of water. It is well-established that porogen may experience chemical instability in exposure to water [57]. Moreover, the stability of porogen in water is affected by contact time [58]. Nevertheless, within the context of this study, it has been assumed that the structural integrity of porogen nanocrystals in water would remain largely unaffected, the given assumption is reasonably accurate due to the low contact time (5 ns). Moreover, the model was used to evaluate the likelihood of PL formation utilizing two widely-used porous solid structures, ZIF-8 and HKUST-1 (Figure 1 and Table 3), as porogens and hydrocarbon liquids including n-pentane, n-octane, iso-octane, cyclohexane, benzene, 1,3,5-trimethyl cyclohexane, 1,3,5-trimethylbenzene, 1,3,5-triisopropylcyclohexane, and 1,3,5-triisopropyl benzene as solvents (Figure 4 and Table 4). These choices represent MOFs with different pore and window sizes and shapes and solvents with different molecular sizes and shapes. The Crystallography Open Database (COD) was used to derive the three-dimensional structures of both ZIF-8 and HKUST-1. Furthermore, all of the solvent structures were prepared by Sketch atom,

and all the simulations were performed by MD simulation in Materials Studio version 17.1.0.48. For clarity, this manuscript follows the naming convention of ‘porogen-solvent’ (e.g., ZIF-8-TEG). Moreover, the initial concentration and the final concentration have been illustrated by  $C_i$  and  $C_f$ .

**Table 3.** Porogens’ structures and their physical properties based on the CoRE MOF Database.

Porogen	CSD CODE	Density (g cm <sup>-3</sup> )	Pore Limiting Diameter (Å)	Largest Cavity Diameter (Å)	Void Fraction	Refs.
ZIF-8	OFERUN07	0.933	3.330	11.392	0.63	[59,60]
HKUST-1	ADABAK	1.640	3.392	3.922	0.392	[60,61]

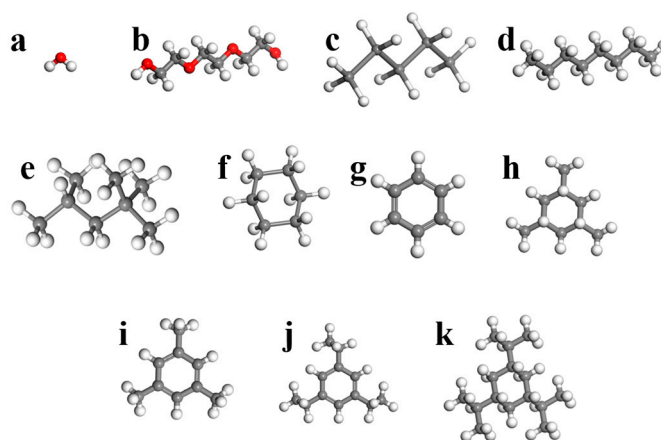


**Figure 4.** Different studied solvents. (a) H<sub>2</sub>O, (b) TEG, (c) n-pentane, (d) n-octane, (e) iso-octane, (f) cyclohexane, (g) benzene, (h) 1,3,5-trimethylcyclohexane, (i) 1,3,5-trimethylbenzene, (j) 1,3,5-triisopropylbenzene, and (k) 1,3,5-triisopropylcyclohexane.

**Table 4.** Solvents characterizations [43].

Solvent	Chemical Formula	Shape	Viscosity (mPa s)	Kinetic Diameter (Å)	Quantum Mechanical	Material Studio Size after MD (Å)		
					QM Diameter (Å)	Length	Height	Depth
Water	H <sub>2</sub> O	Ellipsoidal	-	2.65	3.20	3.93	3.32	3.04
Triethylene glycol	C <sub>6</sub> H <sub>14</sub> O <sub>4</sub>	Prolate rod cylinder	47.8	-	7.89	14.00	4.77	4.25
n-pentane	C <sub>5</sub> H <sub>12</sub>	Prolate rod cylinder	0.224	4.522	6.46	9.19	4.57	4.17
n-octane	C <sub>8</sub> H <sub>18</sub>	Prolate rod cylinder	0.5624	4.537	7.76	13.09	4.80	4.17
iso-octane	C <sub>8</sub> H <sub>18</sub>	Rectangular	0.51	6.2	7.31	8.97	6.51	6.35
Cyclohexane	C <sub>6</sub> H <sub>12</sub>	Spherical	0.89	6.7	6.27	6.61	6.71	5.32
Benzene	C <sub>6</sub> H <sub>6</sub>	Oblate disk cylinder	0.5279	5.85	5.99	6.75	6.72	3.40
1,3,5-trimethylcyclohexane	C <sub>9</sub> H <sub>18</sub>	Triangular	-	-	7.55	6.61	6.71	5.32
1,3,5-trimethylbenzene	C <sub>9</sub> H <sub>12</sub>	Triangular	0.727	-	7.61	8.38	8.33	4.07
1,3,5-triisopropylcyclohexane	C <sub>15</sub> H <sub>30</sub>	Triangular	-	-	9.41	9.12	7.81	4.58
1,3,5-triisopropylbenzene	C <sub>15</sub> H <sub>24</sub>	Triangular	-	-	9.50	10.60	9.72	6.72

### Measuring Open Porosity

The mean square displacement (MSD) diagram, which can be obtained in the software, demonstrates the solvents' mobility and hence the likelihood of penetration under the necessary circumstances. The greater the mobility, the greater the probability of penetration [9]. The presence of open porosity in the systems was confirmed using visual observation and the concentration profile. The position of the solvent molecules and their presence or absence in the porous structure are analyzed at the end of the simulations using the comparison between initial and final snapshots [38]. At both the beginning and the end of the simulation, the concentration profile is utilized to carry out a check on the concentration of solvent molecules at every specific location [62].

## 3. Results and Discussion

Type II/III PLs must prevent the entrance of solvents into porogen pores. The shape and size of the pore aperture must be bigger than the solvent molecule for solvent penetration to occur, while gas molecules may enter the pores. However, size and shape alone are insufficient to predict PL formation; the partial penetration of solvent molecules must also be considered. Therefore, an MD model was developed to evaluate the likelihood of PL formation using a selected porogen and solvent prior to doing the experiment as a readily accessible and cost-effective strategy.

### 3.1. Model Validation

In order to validate the force field for solvents, H<sub>2</sub>O and TEG densities were calculated at 293.15 K and 1 atm using a primary simulation with an NPT ensemble (all of the settings were kept like the main simulation). Table 5 displays the comparison between the obtained and reference density values of the pure solvents. As the error percentages were minimal, the force field can be applied to H<sub>2</sub>O and TEG molecules in the simulations. Moreover, the obtained and reference density values of the other solvents were compared, and it was determined that the force field can be applied to all of them.

**Table 5.** The comparison between the obtained and reference density values of the pure solvents.

Solvent	Simulation Density (g cm <sup>-3</sup> )	References Density (g cm <sup>-3</sup> )	Error (%)	Ref.
Water	0.9972	0.9982	0.1001	-
Triethylene glycol	1.1267	1.1274	0.06204	[63]
n-pentane	0.6238	0.626	0.3514	[64]
n-octane	0.698	0.703	0.7112	[65]
iso-octane	0.6944	0.6919	0.3613	[65]
Cyclohexane	0.7735	0.7781	0.5911	[63]
Benzene	0.8732	0.8790	0.6598	[65]
1,3,5-trimethylcyclohexane	0.7172	0.7180	0.1114	[63]
1,3,5-trimethylbenzene	0.8593	0.8637	0.5094	[63]
1,3,5-triisopropylcyclohexane	0.7951	0.8000	0.6125	[66]
1,3,5-triisopropylbenzene	0.8415	0.8447	0.3788	[31]

In order to evaluate the equilibrium state of the system, an analysis was conducted by examining the total energy of the system comprising solvent molecules within the simulation box. As depicted in Figure 5, the total energy diagrams of the system over a 500 ps period of energy relaxation are presented. Since the temperature is artificially controlled by the thermostat, the total energy fluctuates around its mean value [9,67]. It is observed that following an initial phase of fluctuation, the total energy reaches a state of stability. This stabilization indicates that the solvent molecules have attained a consistent state with the system's stability. The convergence of the total energy towards a stable value implies a uniform distribution of solvent molecules throughout the system, characteristic of a system in equilibrium, where the total energy remains relatively constant over time.

It must be noted that the focus on the system's stability, particularly concerning solvent distribution, does not directly delve into the adsorption equilibrium of molecules within ZIF-8 and HKUST-1 [68–70].

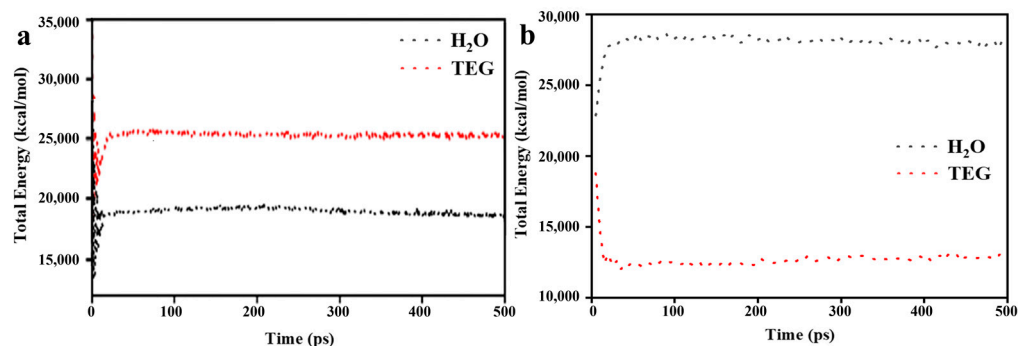


**Figure 5.** Total energy diagrams as a function of time during the energy relaxation of (a) ZIF-8-H<sub>2</sub>O and ZIF-8-TEG and (b) HKUST-1-H<sub>2</sub>O and HKUST-1-TEG combinations.

The scientific literature indicates that H<sub>2</sub>O and TEG molecules are incapable of penetrating ZIF-8 pores, and this combination forms a stable PL [31,71,72]. Furthermore, several studies have demonstrated significant penetration of H<sub>2</sub>O and TEG molecules in HKUST-1 [73–75]. Therefore, the model was validated using simulations employing ZIF-8 and HKUST-1 as the porogens and H<sub>2</sub>O and TEG as the solvents.

The MSD diagrams of H<sub>2</sub>O and TEG molecules in the ZIF-8 structure (Figure 6a) demonstrated the high mobility of the solvents and hence a likelihood of penetration under the necessary circumstances. The greater the mobility, the greater the probability of penetration. Hence, H<sub>2</sub>O molecules are more likely to penetrate than TEG molecules. However, as can be seen in the final snapshots, shown in Figure 7a,b, visual observation confirms that H<sub>2</sub>O and TEG molecules cannot penetrate the ZIF-8 pores. Moreover, the concentration profile in Figure 8a indicates the absence of H<sub>2</sub>O and TEG molecules in the 16.9 to 33.8 Å region which confirms the inability of H<sub>2</sub>O and TEG molecules penetration into the ZIF-8 pores [28,31,53,58]. According to the MSD diagrams of H<sub>2</sub>O and TEG molecules at the HKUST structure, which were large compared to the associated values in ZIF-8, Figure 6b, the solvents have high mobility and are thus more likely to penetrate under the required conditions. In addition, since H<sub>2</sub>O molecules are more mobile than TEG molecules, they are more likely to penetrate. As shown in Figure 7c,d, the visual observation demonstrates the penetration of H<sub>2</sub>O and TEG molecules in HKUST-1 pores. In addition, the concentration profile, shown in Figure 8b, reveals the presence of H<sub>2</sub>O and TEG molecules in the 26.3 to 52.6 Å region, confirming that H<sub>2</sub>O and TEG molecules have penetrated the HKUST-1 pores [73–75]. These results align with those reported in the literature, demonstrating that the model has been validated.

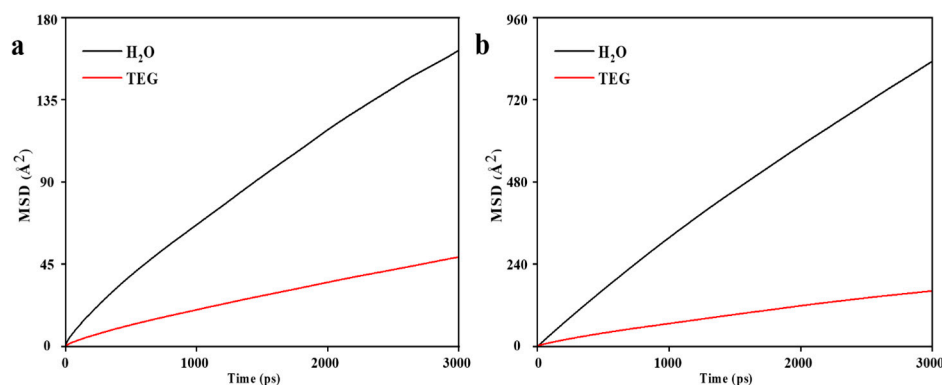


**Figure 6.** MSD diagrams of H<sub>2</sub>O and TEG molecules as a function of time for (a) ZIF-8-H<sub>2</sub>O and ZIF-8-TEG and (b) HKUST-1-H<sub>2</sub>O and HKUST-1-TEG combinations.

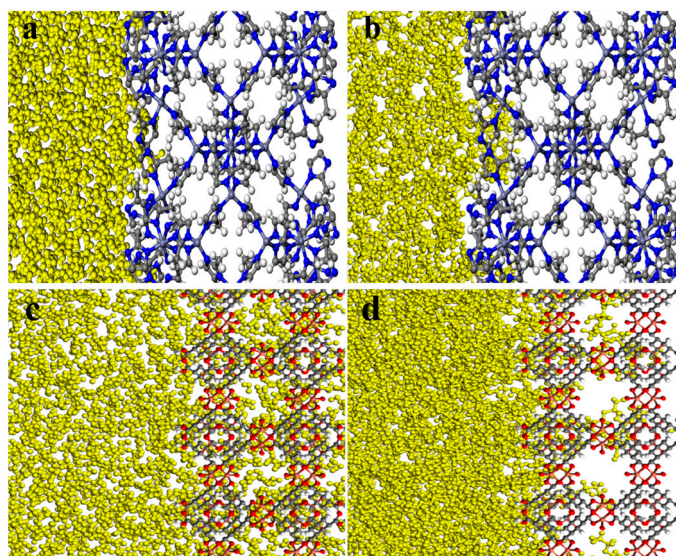


**Figure 7.** The final snapshots of ZIF-8 with (a) H<sub>2</sub>O and (b) TEG molecules and HKUST-1 with (c) H<sub>2</sub>O and (d) TEG molecule combinations.

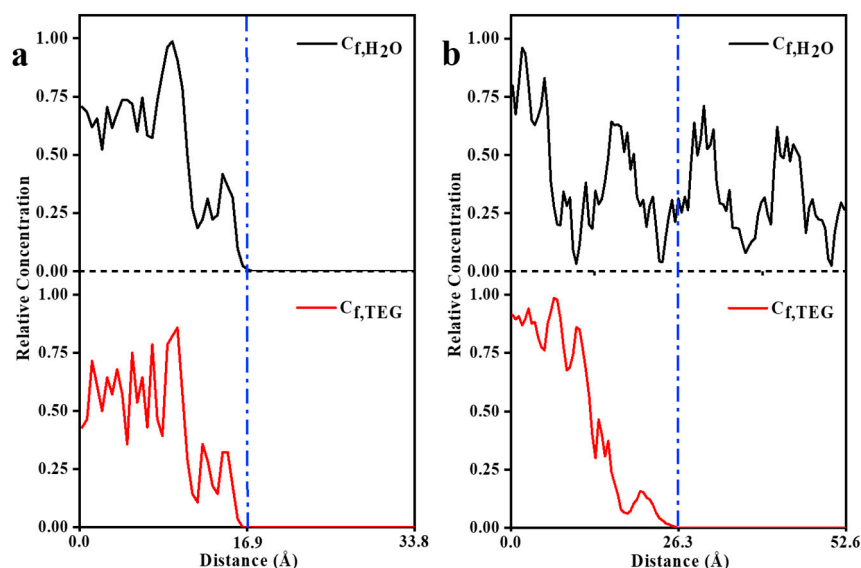


**Figure 8.** Relative concentration profiles of (a) ZIF-8-H<sub>2</sub>O and ZIF-8-TEG and (b) HKUST-1-H<sub>2</sub>O and HKUST-1-TEG combinations (the blue dashed line represents the interface between the solvent and the MOF).

### 3.2. MD Model

The preparation of type II and III PLs involves dissolving or dispersing porogens in a solvent that sterically hinders the porogens from entering the pores, respectively. Consequently, the porogens innate porosity is preserved by blocking the solvent's access to the porogen [72]. In addition, because of the presence of a solvent in type II or III PLs, the porogen system must be robust and stable, incapable of collapsing when surrounded by a solvent or devoid of guest molecules [12,76]. A small porogen window could be used to use the size and shape exclusion principle to accomplish all of these [77]. Furthermore, there are certain parameters that the solvent must meet for PLs to form. For instance, the biggest windows of the porogen should be smaller than the minimum dimension of the solvent. Therefore, as can be seen in Figure 9, the molecular size must be considered while selecting a solvent to prevent solvent penetrability into porogen pores [12,28,78,79]. However, when it is thermodynamically favorable for solvent molecules to interact with

other solvent molecules rather than to fill the porogen networks, the porogens will be left unfilled. Hence, it is possible to form a PL with a solvent that is smaller than the porogen's window [80,81]. However, these PLs seem to be weaker than conventional PLs because they form looser PLs, and solvents may enter the pores when the pressure is elevated [80].

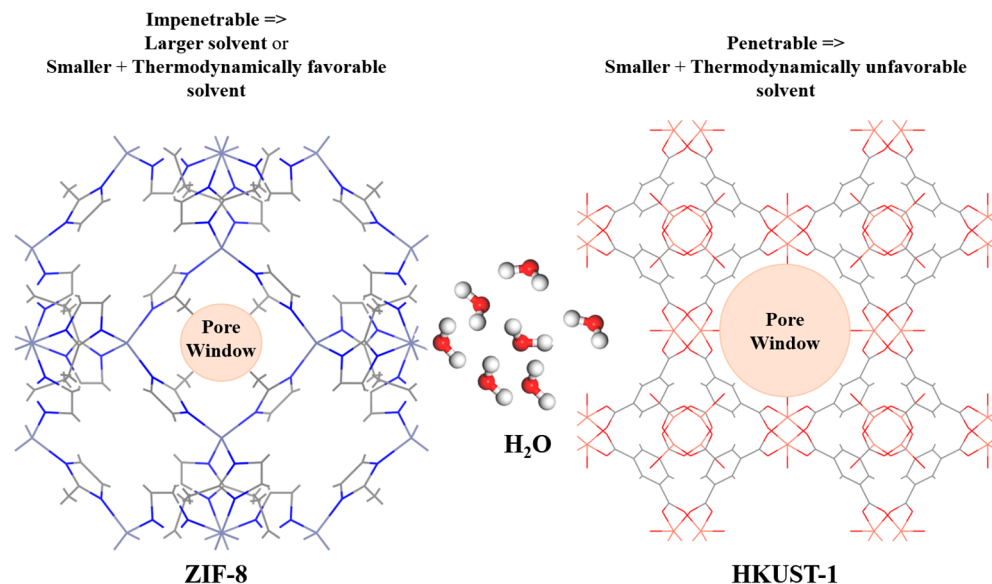


**Figure 9.** The effect of solvent size on penetration.

The kinetic diameter described by empirical data or the quantum mechanically determined diameter explains the penetrability of a solvent whose shape in a 2D plan is regular (such as spherical, ellipsoidal, and prolate rod cylinder), but not when the shape is irregular (such as triangular, oblate disk cylinder, rectangular, branched, and no particular shapes) [82]. In this particular instance, the two smallest dimensions of three must be considered. Moreover, the solvent penetration shape and the 3D shape should be incompatible with the porogen window shape [43]. Indeed, as illustrated in Figure 10, the solvent's ability to enter porogens is affected by both the solvent's shape and size, which also includes the solvent's aspect ratio (solvent's longer side to shorter side) and bulkiness [83]. A linear solvent becomes bulkier through the extension of linear and iso-linear chains. However, the former leads to an aspect ratio far from 1, while the latter causes an aspect ratio closer to 1. As the structure of the solvent changes to an alicyclic one or an aromatic one, the solvent becomes bulkier, and the aspect ratio approaches 1. The stronger the bond, the shorter it will be, and hence, aromatic solvents have a smaller size than alicyclic solvents owing to the existence of double bonds, which are shorter than single bonds.

As shown in Figure 11, in the case of solvents with branches, branch size becomes more crucial since the branch itself may be capable of penetrating pores. Although the addition of branches to alicyclic and aromatic solvents and even branch extensions cause solvents to become bulkier, the aspect ratio is approaching 1. Due to an aspect ratio greater than 1, linear branches are more capable of penetrating than non-linear ones [84]. Generally, solvents with an aspect ratio closer to 1 (regular shape) tend to have a larger penetration shape than those with an aspect ratio farther from 1 (irregular shape), and vice versa. Thus, restriction sizes are often less for solvents with regular shapes and bigger for those with irregular shapes. However, the bulkiness of the solvent remains the most critical variable in influencing solvent penetration through porogen pores [25].

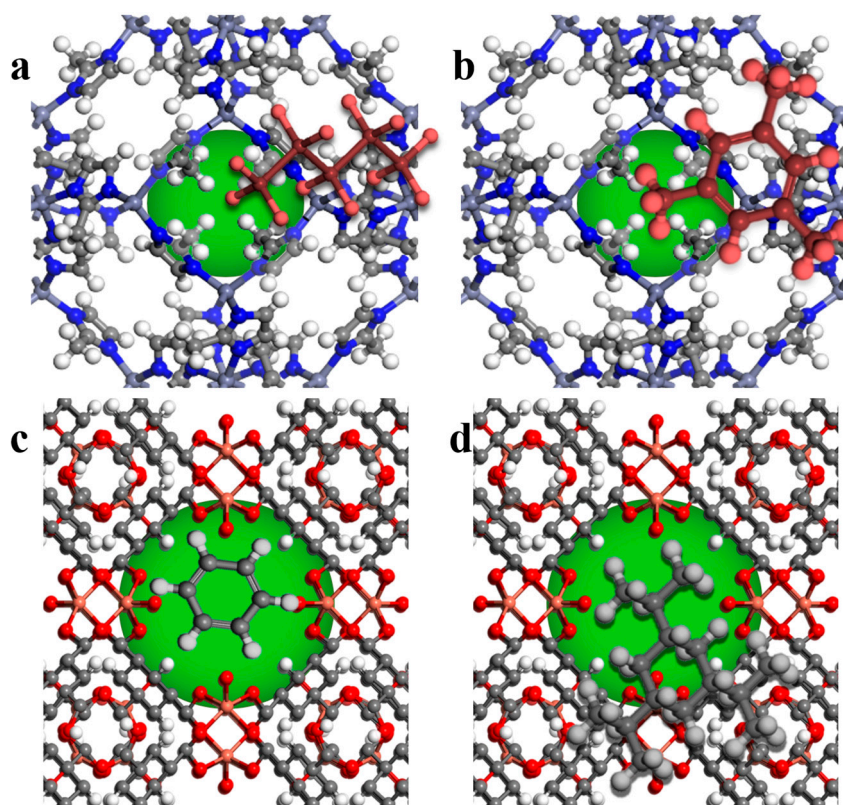


**Figure 10.** The effect of solvent and pore window shapes on partial and complete penetrations in (a) ZIF-8-n-pentane, (b) ZIF-8-1,3,5-trimethylbenzene, (c) HKUST-1-benzene, and (d) HKUST-1-1,3,5-triisopropylcyclohexane (green circles serve as a demonstration of the cavity).

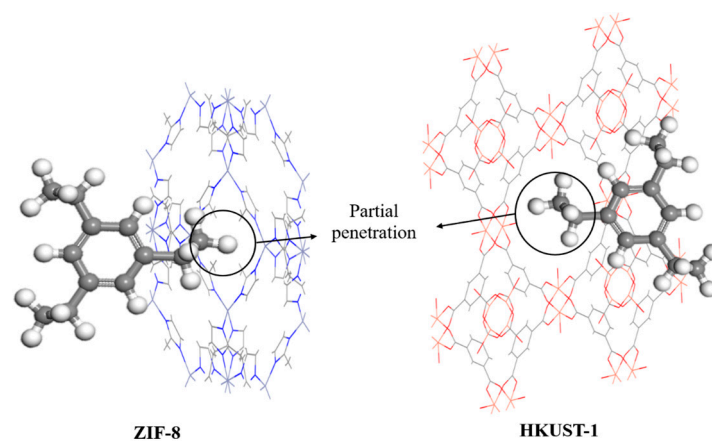


**Figure 11.** Effect of the solvent molecule with branches shape (e.g., 1,3,5-triisopropylcyclohexane) on partial penetration.

The total energy diagrams of the systems during the 500 ps of energy relaxation are illustrated in Figure 12a,b for ZIF-8-solvent combinations and HKUST-1-solvent combinations, respectively. The convergence of the systems' total energy to a constant value demonstrated that they were in equilibrium. This equilibrium allows for the performing of other analyses.

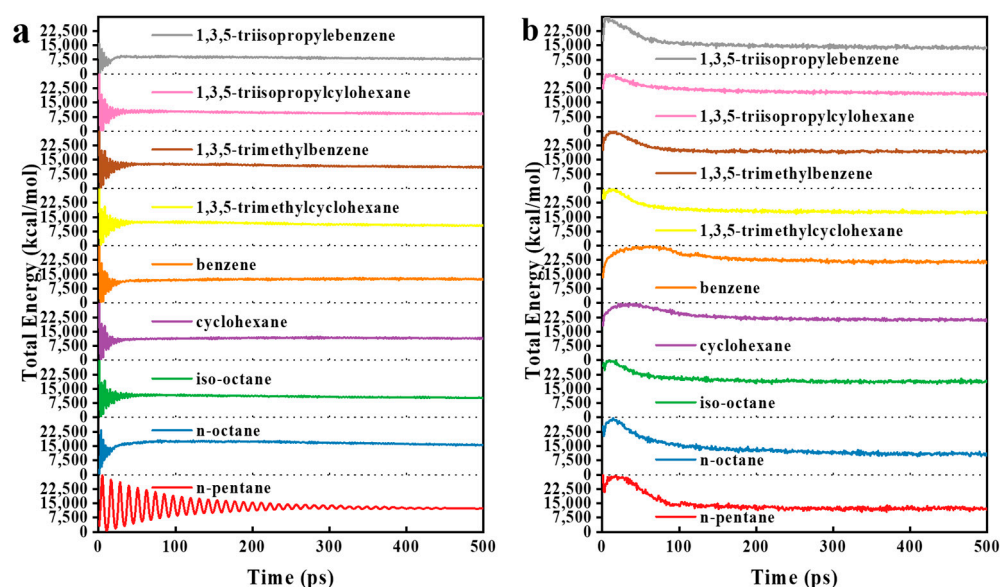


**Figure 12.** Total energy diagrams as a function of time during the energy relaxation for (a) ZIF-8-solvent combinations and (b) HKUST-1-solvent combinations.

The MSD diagrams of all the individual solvent molecules in the ZIF-8 and HKUST-1 combinations are presented in Figure 13. As shown, the penetration of solvents into pores is greater for HKUST-1 than for ZIF-8 due to the high mobility of the solvents. Additionally, the slope of the MSD curve (which is the key factor for mobility) is affected by both the size and shape of the solvent molecules. For example, in HKUST-1, the disk-shaped benzene molecule is more mobile than the linear normal octane molecule. As expected, the mobility for HKUST-1 is consistently higher than those for ZIF-8, supporting the conclusion of greater solvent penetration within HKUST-1. This aligns well with the trends observed in the initial slopes of the MSD curves (Figure 13). Looking at specific examples, n-pentane and n-octane have similar shapes with only slight dimensional differences. Their mobility in HKUST-1 is indeed quite similar, with n-pentane having a slightly higher value due to its smaller size, which allows for easier penetration. Benzene, with its oblate disk cylinder shape, exhibits excellent penetration due to its compatibility with the pore window size (one dimension being only 3.4 angstrom) and its overall smaller size. Similarly, the rectangular shape of isooctane facilitates its penetration into HKUST-1 pores. On the other hand, the triangular-shaped solvent molecules were unable to penetrate either ZIF-8 or HKUST-1, as their dimensions are not compatible with the pore geometries. Additionally, the spherical cyclohexane molecule, with its largest dimension being 6.27 angstrom, also could not penetrate due to size limitations. As seen in Figure 14, the visual observations using the final snapshots of ZIF-8-solvent combinations substantiate that not a single molecule of any of the solvents was able to completely penetrate the ZIF-8 structure. Moreover, Figure 15 illustrates the final snapshots of HKUST-1-solvent combinations. Visual observations verify that the molecules of n-pentane, n-octane, iso-octane, and benzene have fully penetrated the HKUST-1 structure. Furthermore, the strong mobility of the solvents, as shown by the MSD diagrams of all the individual solvent molecules in the HKUST-1 structure, indicated that penetration was possible under the right conditions. In addition, four mentioned solvents, including n-pentane, n-octane, iso-octane, and benzene, had very high mobilities compared to the other solvents, which increased their penetration possibility further than molecules of other solvents. In contrast, the HKUST-1 structure exhibited impenetrability to all other solvents. In addition, the concentration profiles in Figure 16a reveal that due to the absence of solvent molecules in the 16.9 to 33.8 Å region, confirming that solvent molecules did not penetrate the ZIF-8 pores. Based on all the results, it can be concluded that ZIF-8, presumably, forms PL in all solvents tested. As can be seen in Figure 16b, the concentration profile similarly reveals the presence of just the aforementioned solvent

molecules in the HKUST-1 region (the ranges of 26.3 to 52.6 Å) and no other solvents. Therefore, it can be inferred that HKUST-1 is suitable for PL formation with all solvents other than n-pentane, n-octane, iso-octane, and benzene. Since ZIF-8's windows are smaller than HKUST-1's, it can form PLs with sterically hindered solvents with a smaller minimum dimension [85]. The inability of the solvents to enter the porogens' pores is due to the restriction size in combination with the incompatible shapes of the solvents relative to the porogens windows [31].

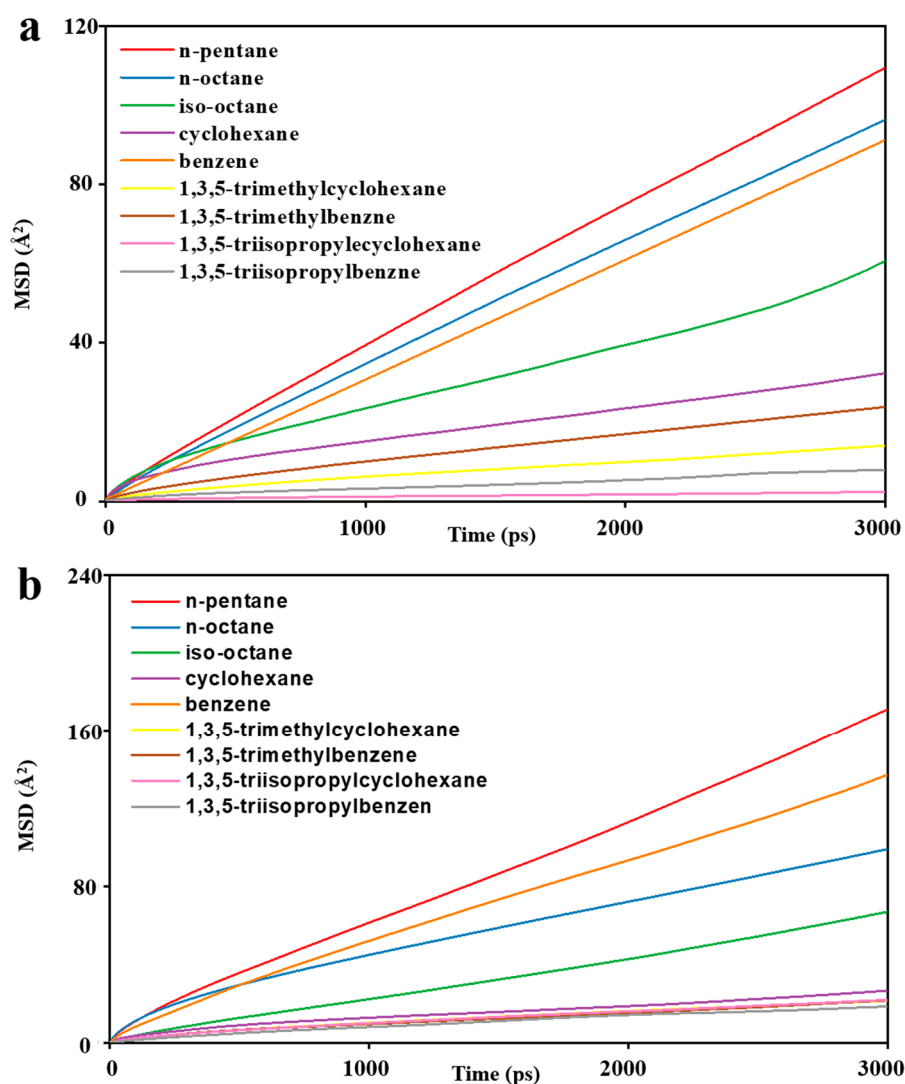


**Figure 13.** MSD diagrams of solvent's molecules as a function of time for (a) ZIF-8-solvent combinations and (b) HKUST-1-solvent combinations.

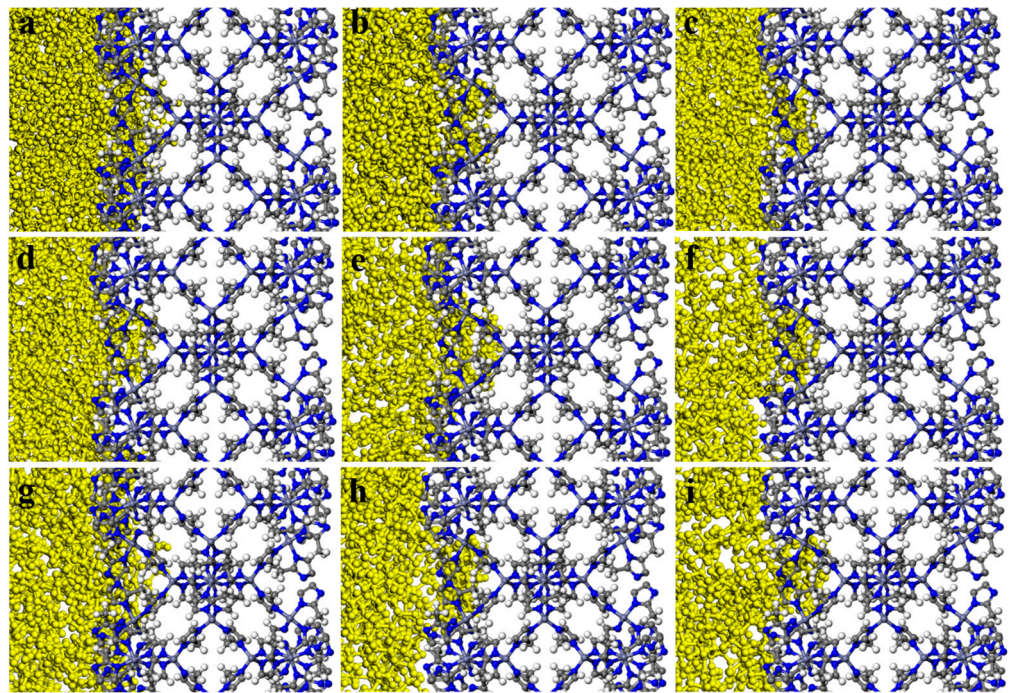


**Figure 14.** Final snapshots of ZIF-8- (a) n-pentane, (b) n-octane, (c) iso-octane, (d) cyclohexane, (e) benzene, (f) 1,3,5-trimethylcyclohexane, (g) 1,3,5-trimethylbenzene, (h) 1,3,5-triisopropylcyclohexane, and (i) 1,3,5-triisopropylbenzene molecules combinations.

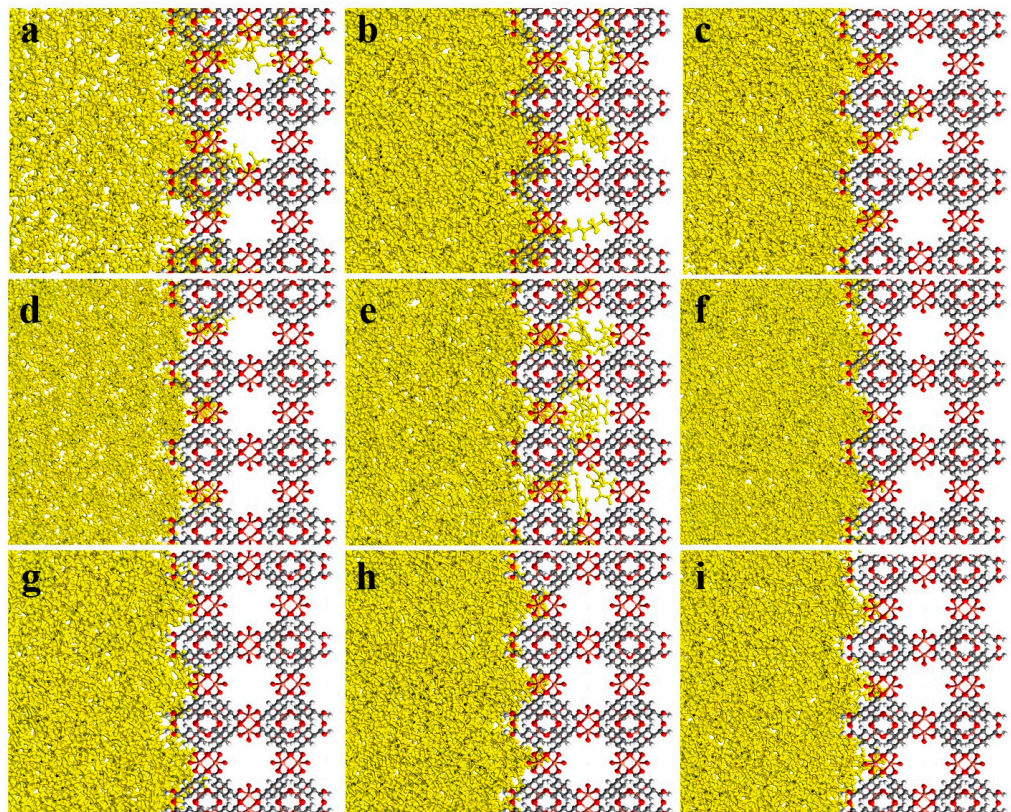


**Figure 15.** Final snapshots of HKUST-1- (a) n-pentane, (b) n-octane, (c) iso-octane, (d) cyclohexane, (e) benzene, (f) 1,3,5-trimethylcyclohexane, (g) 1,3,5-trimethylbenzene, (h) 1,3,5-triisopropylcyclohexane, and (i) 1,3,5-triisopropylbenzene molecules combinations.

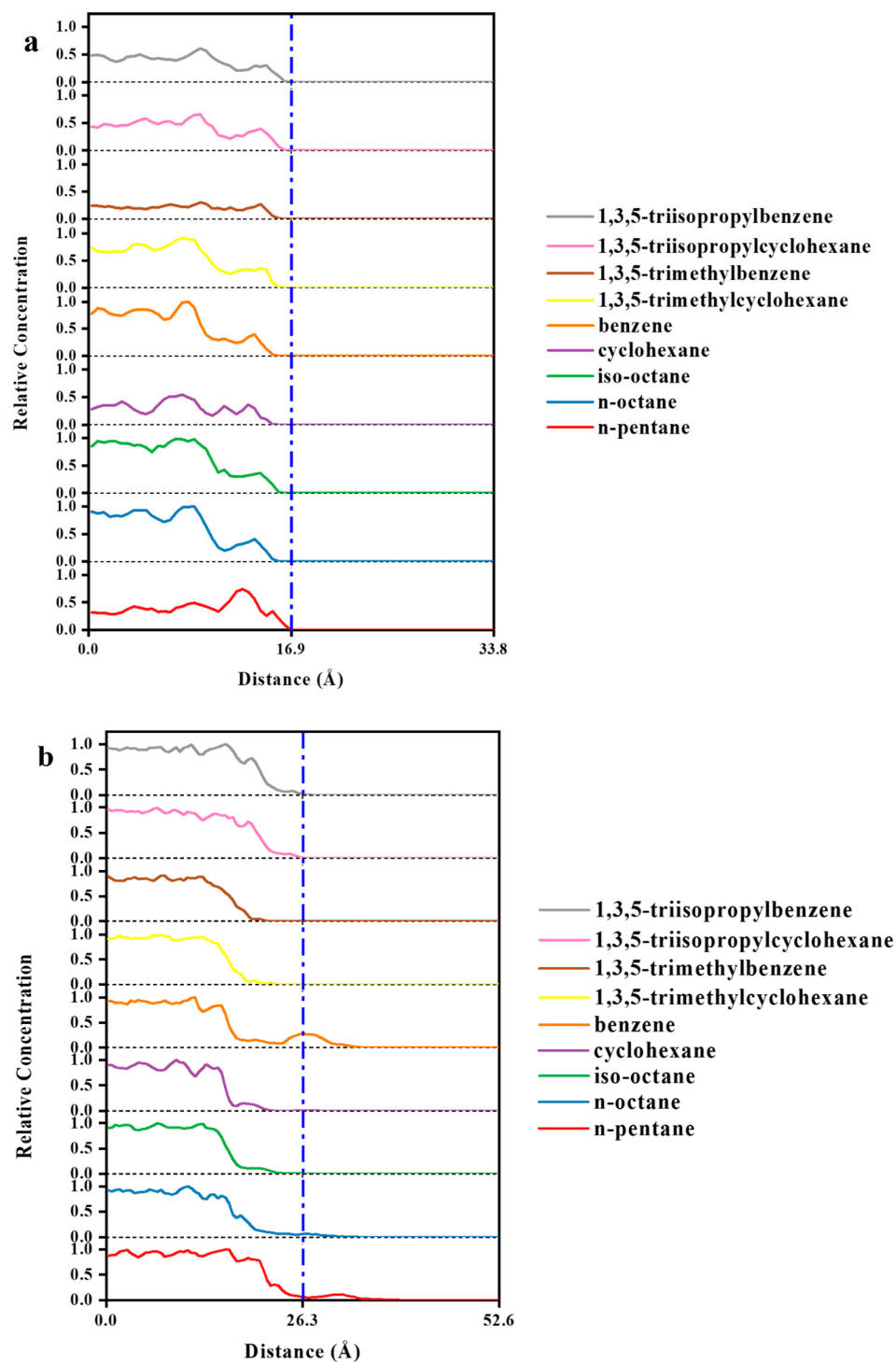


**Figure 16.** Relative concentration profiles of (a) ZIF-8-solvent combinations and (b) HKUST-1-solvent combinations.

It is also noteworthy that based on the visual observation by zooming in further and evaluating the ZIF-8-solvent interface from a closer perspective, Figures 17 and 18, and the concentration profile, Figure 19, it can be observed in some suitable porogen-solvent combinations that a limited amount of partial penetration took place. It was observed that for ZIF-8-solvent combinations, n-pentane has the most partial penetration due to the small size and aspect ratio far from 1. Both n-octane and iso-octane were bulkier, and hence the partial penetration was reduced; although, the former's aspect ratio deviates farther from 1 than the latter. Therefore, the partial penetration of n-octane was larger

than iso-octane. It is noteworthy that despite having an aspect ratio close to 1, benzene displayed partial penetration owing to its small size, while 1,3,5-trimethylbenzene showed even higher partial penetration due to the existence of linear branches. None of the other solvents showed any signs of being able to penetrate just partially. It was found that for HKUST-1-solvent combinations, despite having an aspect ratio close to 1, cyclohexane displayed partial penetration owing to its small size. Although 1,3,5-trimethylbenzene and 1,3,5-trimethyl cyclohexane exhibited partial penetration owing to linear branches (the former more than the latter due to the smaller size), they exhibited less partial penetration due to greater bulkiness and an aspect ratio close to 1 in comparison to the previous solvent. 1,3,5-triisopropyl benzene and 1,3,5-triisopropyl cyclohexane solvents exhibited the same behavior as the previous two solvents but with less partial penetration due to the non-linear branches. Since ZIF-8 has narrower windows than HKUST-1, sterically hindered solvents are less likely to penetrate it partially, and only a small number of solvents can do so. Solvents having an aspect ratio far from 1 and/or solvents with more linear branches are able to partially penetrate the pores of porogens.

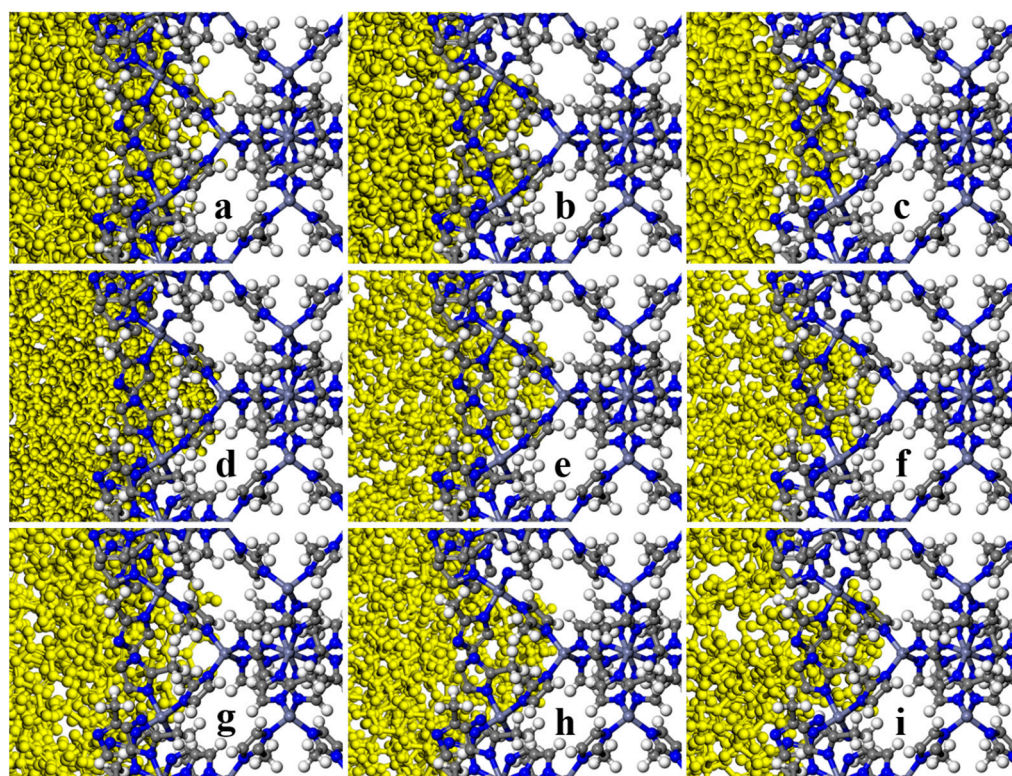


**Figure 17.** A closer look at final snapshots of ZIF-8- (a) n-pentane, (b) n-octane, (c) iso-octane, (d) cyclohexane, (e) benzene, (f) 1,3,5-trimethylcyclohexane, (g) 1,3,5-trimethylbenzene, (h) 1,3,5-triisopropylcyclohexane, and (i) 1,3,5-triisopropylbenzene molecules combinations.

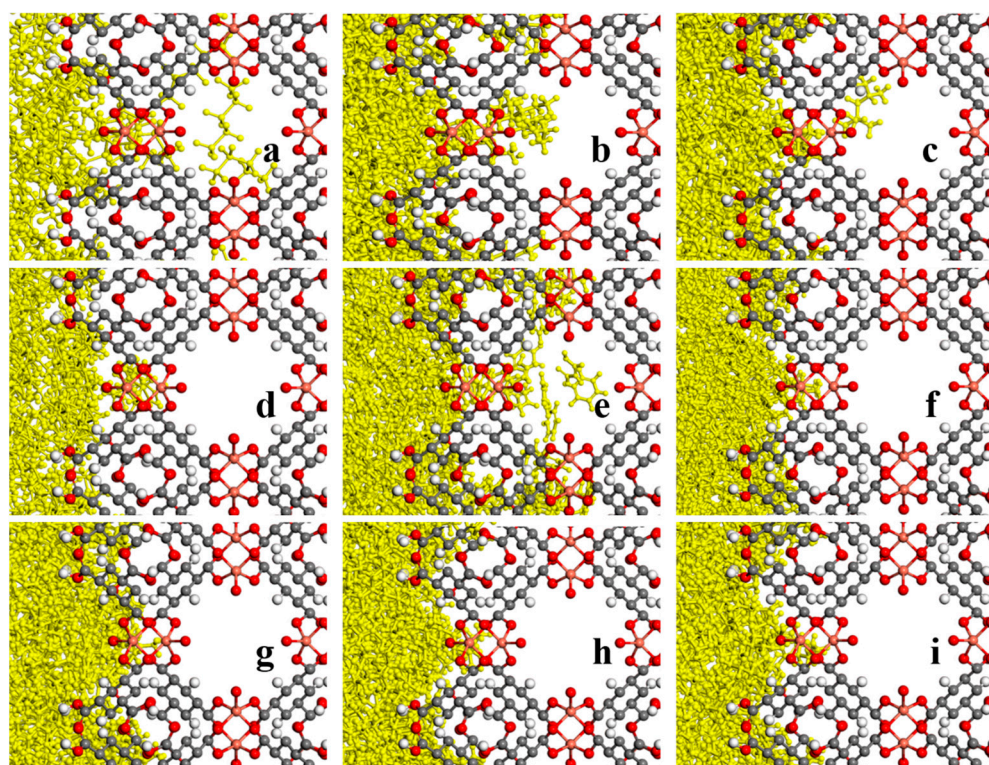


**Figure 18.** A closer look at final snapshots of HKUST-1- (a) n-pentane, (b) n-octane, (c) iso-octane, (d) cyclohexane, (e) benzene, (f) 1,3,5-trimethyl cyclohexane, (g) 1,3,5-trimethyl benzene, (h) 1,3,5-triisopropyl cyclohexane, and (i) 1,3,5-triisopropyl benzene molecules combinations.

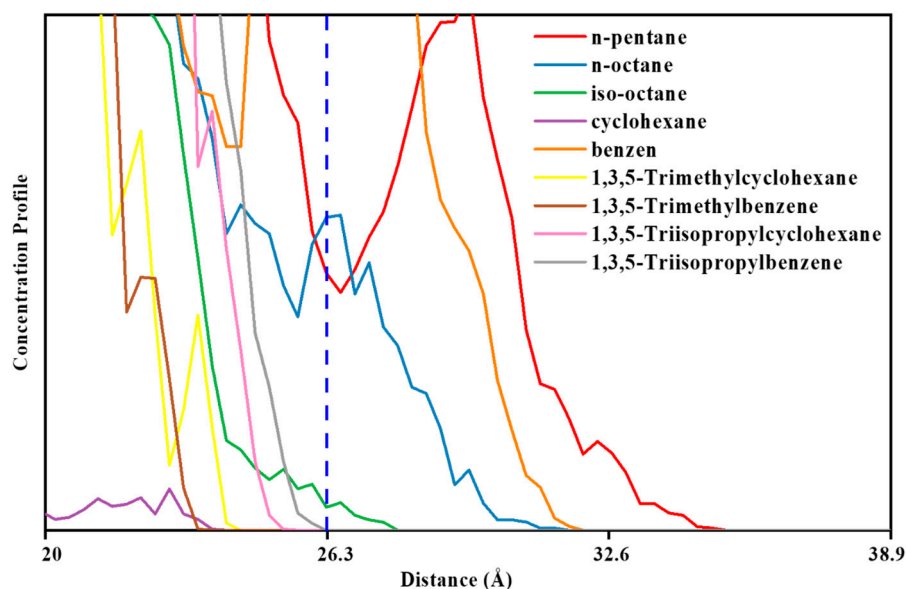


**Figure 19.** A closer look at the relative concentration profiles of HKUST-1-solvent combinations.

#### 4. Conclusions

This study successfully developed an MD model for assessing the possibility of type II/III PLs formation. The model's effectiveness was validated through simulations employing ZIF-8 and HKUST-1 as porogens and H<sub>2</sub>O/TEG as solvents. The simulations demonstrated that the size and shape of the solvent molecules play a crucial role in penetration. H<sub>2</sub>O and TEG were incapable of penetrating the ZIF-8 pores due to their small size and irregular shape. However, both solvents easily penetrated the larger pores of HKUST-1.

Expanding the model's scope, the possibility of PL formation was investigated using ZIF-8 and HKUST-1, which had pores and windows of diverse sizes and shapes, with a wide range of hydrocarbon solvents with distinct dimensions and shapes. The results unveiled a significant discovery: ZIF-8, in contrast to HKUST-1, is capable of forming PLs with a wider variety of sterically hindered solvents due to its smaller apertures. On the contrary, the larger apertures in HKUST-1 permit complete penetration of certain solvents (e.g., benzene, iso-octane, n-pentane), thereby preventing the formation of PL in these particular combinations. This underscores the significance of pore size and aperture size/shape considerations in porogen selection for PL formations. Although defect-free porogens were used in this study, it is crucial to recognize that porogens synthesized in real-world situations inevitably include defects. Therefore, future studies should prioritize the incorporation of these defects into the model to evaluate their impact on the development of PL. This approach can provide a more realistic representation of PL behavior in real conditions, thereby closing the gap between theoretical predictions and experimental results.

**Author Contributions:** H.F. led the project administration, conceptual and simulation design, simulation tuning and optimization, interpretation of results, and writing of the draft; M.R. and H.M. contributed to the project administration, conceptual and simulation design, analysis, and interpretation of results; S.N. contributed to the simulation tuning and optimization. All authors have read and agreed to the published version of the manuscript.

**Funding:** This research received no external funding.

**Data Availability Statement:** Data are unavailable due to privacy and ethical restrictions.

**Conflicts of Interest:** The authors declare no conflicts of interest.

## References

1. Seader, J.D.; Henley, E.J.; Roper, D.K. *Separation Process Principles*; Wiley: New York, NY, USA, 1998; Volume 25.
2. Yaumi, A.L.; Bakar, M.Z.A.; Hameed, B.H. Recent advances in functionalized composite solid materials for carbon dioxide capture. *Energy* **2017**, *124*, 461–480. [[CrossRef](#)]
3. Giri, N.; Del Pópolo, M.G.; Melaugh, G.; Greenaway, R.L.; Rätzke, K.; Koschine, T.; Pison, L.; Gomes, M.F.C.; Cooper, A.I.; James, S.L. Liquids with permanent porosity. *Nature* **2015**, *527*, 216–220. [[CrossRef](#)]
4. Zhang, J.; Chai, S.H.; Qiao, Z.A.; Mahurin, S.M.; Chen, J.; Fang, Y.; Wan, S.; Nelson, K.; Zhang, P.; Dai, S. Porous liquids: A promising class of media for gas separation. *Angew. Chem.* **2015**, *127*, 946–950. [[CrossRef](#)]
5. Bates, E.D.; Mayton, R.D.; Ntai, I.; Davis, J.H. CO<sub>2</sub> Capture by a Task-Specific Ionic Liquid. *J. Am. Chem. Soc.* **2002**, *124*, 926–927. [[CrossRef](#)]
6. Abánades Lázaro, I.; Haddad, S.; Sacca, S.; Orellana-Tavra, C.; Fairen-Jimenez, D.; Forgan, R.S. Selective Surface PEGylation of UiO-66 Nanoparticles for Enhanced Stability, Cell Uptake, and pH-Responsive Drug Delivery. *Chem* **2017**, *2*, 561–578. [[CrossRef](#)]
7. Siegel, R.W.; Hu, E.; Cox, D.M.; Goronkin, H.; Jelinski, L.; Koch, C.C.; Mendel, J.; Roco, M.C.; Shaw, D.T. (Eds.) *Nanostructure Science and Technology: R&D Status and Trends in Nanoparticles, Nanostructured Materials, and Nanodevices*; Springer: Dordrecht, The Netherlands, 1999; pp. 49–66.
8. Armand, M.; Endres, F.; MacFarlane, D.R.; Ohno, H.; Scrosati, B. Ionic-liquid materials for the electrochemical challenges of the future. *Nat. Mater.* **2009**, *8*, 621–629. [[CrossRef](#)]
9. Zhang, F. Thermodynamics and kinetics of gas storage in porous liquids. *Phys. Chem. B* **2016**, *120*, 7195–7200. [[CrossRef](#)]
10. Greenaway, R.L.; Holden, D.; Eden, E.G.; Stephenson, A.; Yong, C.W.; Bennison, M.J.; Hasell, T.; Briggs, M.E.; James, S.L.; Cooper, A.I. Understanding gas capacity, guest selectivity, and diffusion in porous liquids. *Chem. Sci.* **2017**, *8*, 2640–2651. [[CrossRef](#)]
11. Fulvio, P.F.; Dai, S. Porous liquids: The next frontier. *Chem* **2020**, *6*, 3263–3287. [[CrossRef](#)]
12. O'Reilly, N.; Giri, N.; James, S.L. Porous liquids. *Chem. Eur. J.* **2007**, *13*, 3020–3025. [[CrossRef](#)]
13. Alexander, F.M.; Fonrouge, S.F.; Borioni, J.L.; Del Pópolo, M.G.; Horton, P.N.; Coles, S.J.; Hutchings, B.P.; Crawford, D.E.; James, S.L. Noria and its derivatives as hosts for chemically and thermally robust Type II porous liquids. *Chem. Sci.* **2021**, *12*, 14230–14240. [[CrossRef](#)]
14. Wang, D.; Xin, Y.; Yao, D.; Li, X.; Ning, H.; Zhang, H.; Wang, Y.; Ju, X.; He, Z.; Yang, Z. Shining light on porous liquids: From fundamentals to syntheses, applications and future challenges. *Adv. Funct. Mater.* **2022**, *32*, 2104162. [[CrossRef](#)]
15. Dinker, M.K.; Zhao, K.; Liu, S.; Qi, S.-C.; Li, Y.-X.; Liu, G.-P.; Ding, L.; Liu, X.-Q.; Sun, L.-B. Permanent cavities in ionic liquids created by metal–organic polyhedra. *J. Mater. Chem. A* **2022**, *10*, 16204–16211. [[CrossRef](#)]
16. Hasell, T.; Cooper, A.I. Porous organic cages: Soluble, modular and molecular pores. *Nat. Rev. Mater.* **2016**, *1*, 16053. [[CrossRef](#)]
17. Ma, L.; Haynes, C.J.; Grommet, A.B.; Walczak, A.; Parkins, C.C.; Doherty, C.M.; Longley, L.; Tron, A.; Stefankiewicz, A.R.; Bennett, T.D. Coordination cages as permanently porous ionic liquids. *Nat. Chem.* **2020**, *12*, 270–275. [[CrossRef](#)]

18. Jie, K.; Onishi, N.; Schott, J.A.; Popovs, I.; Jiang, D.E.; Mahurin, S.; Dai, S. Transforming porous organic cages into porous ionic liquids via a supramolecular complexation strategy. *Angew. Chem.* **2020**, *132*, 2288–2292. [[CrossRef](#)]
19. Li, H.; Liu, B.; Yang, M.; Zhu, D.; Huang, Z.; Chen, W.; Yang, L.; Chen, G. CO<sub>2</sub> separation performance of zeolitic imidazolate framework-8 porous slurry in a pilot-scale packed tower. *Ind. Eng. Chem. Res.* **2020**, *59*, 6154–6163. [[CrossRef](#)]
20. Boveni, M.; Mauri, M.; Alexander, F.; James, S.L.; Simonutti, R.; Castiglione, F. Exploring cavities in Type II porous liquids with xenon. *J. Mol. Liq.* **2023**, *370*, 121038. [[CrossRef](#)]
21. Smith, S.J.; Wood, C.D.; Feron, P.H.; Mahdavi, H.; Mulder, R.J.; Doherty, C.M.; Hill, M.R.; Mulet, X. Porous solid inspired hyper-crosslinked polymer liquids with highly efficient regeneration for gas purification. *Sci. China Mater.* **2022**, *65*, 1937–1942. [[CrossRef](#)]
22. Hosseini Monjezi, B.; Kutonova, K.; Tsotsalas, M.; Henke, S.; Knebel, A. Current trends in metal–organic and covalent organic framework membrane materials. *Angew. Chem. Int. Ed.* **2021**, *60*, 15153–15164. [[CrossRef](#)]
23. Mahdavi, H.; Eden, N.T.; Doherty, C.M.; Acharya, D.; Smith, S.J.; Mulet, X.; Hill, M.R. Underlying Polar and Nonpolar Modification MOF-Based Factors that Influence Permanent Porosity in Porous Liquids. *ACS Appl. Mater. Interfaces* **2022**, *14*, 23392–23399. [[CrossRef](#)]
24. Shan, W.; Fulvio, P.F.; Kong, L.; Schott, J.A.; Do-Thanh, C.-L.; Tian, T.; Hu, X.; Mahurin, S.M.; Xing, H.; Dai, S. New class of type III porous liquids: A promising platform for rational adjustment of gas sorption behavior. *ACS Appl. Mater. Interfaces* **2018**, *10*, 32–36. [[CrossRef](#)]
25. Cahir, J.; Tsang, M.Y.; Lai, B.; Hughes, D.; Alam, M.A.; Jacquemin, J.; Rooney, D.; James, S.L. Type 3 porous liquids based on non-ionic liquid phases—a broad and tailorable platform of selective, fluid gas sorbents. *Chem. Sci.* **2020**, *11*, 2077–2084. [[CrossRef](#)]
26. Bavykina, A.; Cadiou, A.; Gascon, J. Porous liquids based on porous cages, metal organic frameworks and metal organic polyhedra. *Coord. Chem. Rev.* **2019**, *386*, 85–95. [[CrossRef](#)]
27. Nakanishi, T. *Functional Organic Liquids*; John Wiley & Sons: Hoboken, NJ, USA, 2019.
28. Mahdavi, H.; Smith, S.J.; Mulet, X.; Hill, M.R. Practical considerations in the design and use of porous liquids. *Mater. Horiz.* **2022**, *9*, 1577–1601. [[CrossRef](#)]
29. Mahdavi, H.; Sadiq, M.M.; Smith, S.J.D.; Mulet, X.; Hill, M.R. Underlying potential evaluation of the real-process applications of magnetic porous liquids. *J. Mater. Chem. A* **2023**, *11*, 16846–16853. [[CrossRef](#)]
30. Mukesh, C.; Sarmad, S.; Samikannu, A.; Nikjoo, D.; Siljebo, W.; Mikkola, J.-P. Pore size-excluded low viscous porous liquids for CO<sub>2</sub> sorption at room temperature and thermodynamic modeling study. *J. Mol. Liq.* **2022**, *356*, 119046. [[CrossRef](#)]
31. Mahdavi, H.; Zhang, H.; Macreadie, L.K.; Doherty, C.; Acharya, D.; Smith, S.J.; Mulet, X.; Hill, M.R. Underlying solvent-based factors that influence permanent porosity in porous liquids. *Nano Res.* **2022**, *15*, 3533–3538. [[CrossRef](#)]
32. Kunde, T.; Pausch, T.; Schmidt, B.M. Porous Organic Compounds—Small Pores on the Rise. *Eur. J. Org. Chem.* **2021**, *2021*, 5844–5856. [[CrossRef](#)]
33. Kearsey, R.J.; Alston, B.M.; Briggs, M.E.; Greenaway, R.L.; Cooper, A.I. Accelerated robotic discovery of type II porous liquids. *Chem. Sci.* **2019**, *10*, 9454–9465. [[CrossRef](#)]
34. Liu, H.; Liu, B.; Lin, L.-C.; Chen, G.; Wu, Y.; Wang, J.; Gao, X.; Lv, Y.; Pan, Y.; Zhang, X. A hybrid absorption–adsorption method to efficiently capture carbon. *Nat. Commun.* **2014**, *5*, 5147. [[CrossRef](#)]
35. Atilhan, M.; Cincotti, A.; Aparicio, S. Nanoscopic characterization of type II porous liquid and its use for CO<sub>2</sub> absorption from molecular simulation. *J. Mol. Liq.* **2021**, *330*, 115660. [[CrossRef](#)]
36. Horstmann, R.; Hecht, L.; Kloth, S.; Vogel, M. Structural and Dynamical Properties of Liquids in Confinements: A Review of Molecular Dynamics Simulation Studies. *Langmuir* **2022**, *38*, 6506–6522. [[CrossRef](#)]
37. Melaugh, G.; Giri, N.; Davidson, C.E.; James, S.L.; Del Pópolo, M.G. Designing and understanding permanent microporosity in liquids. *Phys. Chem. Chem. Phys.* **2014**, *16*, 9422–9431. [[CrossRef](#)]
38. Costa Gomes, M.; Pison, L.; Červinka, C.; Padua, A. Porous ionic liquids or liquid metal–organic frameworks? *Angew. Chem.* **2018**, *130*, 12085–12088. [[CrossRef](#)]
39. Sheng, L.; Chen, Z.; Wang, Y. Molecular dynamics simulations of stability and fluidity of porous liquids. *Appl. Surf. Sci.* **2021**, *536*, 147951. [[CrossRef](#)]
40. Sheng, L.; Chen, Z.; Xu, B.; Shi, J. Molecular dynamics study of the dispersion stability and fluidity of porous liquids with different canopy structures. *J. Phys. Chem. B.* **2021**, *125*, 5387–5396. [[CrossRef](#)]
41. Avila, J.; Červinka, C.; Dugas, P.Y.; Pádua, A.A. Costa Gomes, M. Porous ionic liquids: Structure, stability, and gas absorption mechanisms. *Adv. Mater. Interfaces* **2021**, *8*, 2001982. [[CrossRef](#)]
42. Zhao, X.; Ding, Y.; Ma, L.; Zhu, X.; Wang, H.; Cheng, M.; Liao, Q. A molecular dynamic insight into CO<sub>2</sub> diffusion of type III porous liquids. *J. Mol. Liq.* **2023**, *389*, 122731. [[CrossRef](#)]
43. Mahdavi, H.; Burdloff, J.; Robin, A.; Smith, S.J.D.; Mulet, X.; Hill, M.R. Accelerated Systematic Investigation of Solvents Suitability for Type II/III Porous Liquids. *ACS Mater. Lett.* **2023**, *5*, 549–557. [[CrossRef](#)]
44. Vendite, A.C.; Soares, T.A.; Coutinho, K. The Effect of Surface Composition on the Selective Capture of Atmospheric CO<sub>2</sub> by ZIF Nanoparticles: The Case of ZIF-8. *J. Chem. Inf. Model.* **2022**, *62*, 6530–6543. [[CrossRef](#)]
45. Mohan, V.; Smith, P.E.; Pettitt, B.M. Molecular dynamics simulation of ions and water around triplex DNA. *J. Phys. Chem.* **1993**, *97*, 12984–12990. [[CrossRef](#)]

46. Zhang, X.; Yi, H.; Zhao, Y.; Min, F.; Song, S. Study on the differences of Na- and Ca-montmorillonites in crystalline swelling regime through molecular dynamics simulation. *J. Phys. Chem.* **2016**, *27*, 779–785. [\[CrossRef\]](#)
47. Addicoat, M.A.; Vankova, N.; Akter, I.F.; Heine, T. Extension of the Universal Force Field to Metal–Organic Frameworks. *J. Chem. Theory Comput.* **2014**, *10*, 880–891. [\[CrossRef\]](#)
48. Zhao, X.; Ding, Y.; Ma, L.; Zhu, X.; Wang, H.; Liao, Q. An enhancement of CO<sub>2</sub> capture in a type-III porous liquid by 2-Methylimidazole zinc salt (ZIF-8). *J. Mol. Liq.* **2022**, *367*, 120523. [\[CrossRef\]](#)
49. Parkes, M.V.; Demir, H.; Teich-McGoldrick, S.L.; Sholl, D.S.; Greathouse, J.A.; Allendorf, M.D. Molecular dynamics simulation of framework flexibility effects on noble gas diffusion in HKUST-1 and ZIF-8. *Microporous Mesoporous Mater.* **2014**, *194*, 190–199. [\[CrossRef\]](#)
50. Paudel, H.P.; Shi, W.; Hopkinson, D.; Steckel, J.A.; Duan, Y. Engineering. Computational modelling of adsorption and diffusion properties of CO<sub>2</sub> and CH<sub>4</sub> in ZIF-8 for gas separation applications: A density functional theory approach. *React. Chem. Eng.* **2021**, *6*, 990–1001. [\[CrossRef\]](#)
51. Zhao, L.; Yang, Q.; Ma, Q.; Zhong, C.; Mi, J.; Liu, D. A force field for dynamic Cu-BTC metal-organic framework. *J. Mol. Model.* **2011**, *17*, 227–234. [\[CrossRef\]](#)
52. Rappé, A.K.; Casewit, C.J.; Colwell, K.; Goddard III, W.A.; Skiff, W.M. UFF, a full periodic table force field for molecular mechanics and molecular dynamics simulations. *J. Am. Chem. Soc.* **1992**, *114*, 10024–10035. [\[CrossRef\]](#)
53. Sheng, L.; Chen, Z. Molecular dynamics study of dispersion and fluidity of porous liquids with different pore sizes. *J. Mol. Liq.* **2021**, *333*, 115890. [\[CrossRef\]](#)
54. Zhang, X.; Huang, T.; Shan, T.; Yuan, Q.; Yin, S.; Li, J.; Wu, Q.; Zhang, P. Molecular dynamics study of the influence of water molecular phase state on the replacement of CO<sub>2</sub>–CH<sub>4</sub> hydrate in porous media. *J. Mol. Liq.* **2023**, *391*, 123401. [\[CrossRef\]](#)
55. Islam, M.A.; Rony, M.D.; Hasan, M.N. Thin film liquid-vapor phase change phenomena over nano-porous substrates: A molecular dynamics perspective. *Heliyon* **2023**, *9*, e15714. [\[CrossRef\]](#)
56. Ferreira, P.H.L.; Sampaio, A.M.; Siqueira, L.J.A. Energy and power performances of binary mixtures of ionic liquids in planar and porous electrodes by molecular dynamics simulations. *Electrochim. Acta* **2022**, *410*, 139982. [\[CrossRef\]](#)
57. Liu, X.; Li, Y.; Ban, Y.; Peng, Y.; Jin, H.; Bux, H.; Xu, L.; Caro, J.; Yang, W. Improvement of hydrothermal stability of zeolitic imidazolate frameworks. *Chem. Commun.* **2013**, *49*, 9140–9142. [\[CrossRef\]](#)
58. Zhang, H.; Zhao, M.; Lin, Y.S. Stability of ZIF-8 in water under ambient conditions. *Microporous Mesoporous Mater.* **2019**, *279*, 201–210. [\[CrossRef\]](#)
59. Morris, W.; Stevens, C.J.; Taylor, R.E.; Dybowski, C.; Yaghi, O.M.; Garcia-Garibay, M.A. NMR and X-ray Study Revealing the Rigidity of Zeolitic Imidazolate Frameworks. *J. Phys. Chem. C* **2012**, *116*, 13307–13312. [\[CrossRef\]](#)
60. Moghadam, P.Z.; Li, A.; Wiggan, S.B.; Tao, A.; Maloney, A.G.P.; Wood, P.A.; Ward, S.C.; Fairen-Jimenez, D. Development of a Cambridge Structural Database Subset: A Collection of Metal–Organic Frameworks for Past, Present, and Future. *Chem. Mater.* **2017**, *29*, 2618–2625. [\[CrossRef\]](#)
61. Xiang, S.; Zhou, W.; Gallegos, J.M.; Liu, Y.; Chen, B. Exceptionally High Acetylene Uptake in a Microporous Metal–Organic Framework with Open Metal Sites. *J. Am. Chem. Soc.* **2009**, *131*, 12415–12419. [\[CrossRef\]](#)
62. Lyons, M.A.; Reisfeld, B.; Yang, R.S.; Lenaerts, A.J. A physiologically based pharmacokinetic model of rifampin in mice. *Antimicrob. Agents Chemother.* **2013**, *57*, 1763–1771. [\[CrossRef\]](#)
63. Budavari, S.; O’Neil, M.; Smith, A.; Heckelman, P.; Kinneary, J. *The Merck Index. An Encyclopedia of Chemicals, Drugs and Biologicals*, 13th ed.; Merck and Co., Inc.: Whitehouse Station, NJ, USA, 2001; Volume 1097, p. 1946.
64. Haynes, W. *CRC Handbook of Chemistry and Physics*, 94th ed.; Internet Version; Taylor & Francis: Boca Raton, FL, USA, 2014.
65. Guard, U.C. *Chemical Hazard Response Information System (CHRIS)–Hazardous Chemical Data*; Technical Report Commandant Instruction 16465.12C; Department of Transportation: Washington, DC, USA, 1999.
66. Bruno, T.J.; Fortin, T.J.; Lovestead, T.M.; Widgren, J.A. Chemical and thermophysical characterization of 1,3,5-triisopropylcyclohexane. *J. Chem. Eng. Data* **2012**, *57*, 2343–2349. [\[CrossRef\]](#)
67. Rajabpour, A.; Akizi, F.Y.; Heyhat, M.M.; Gordiz, K. Molecular dynamics simulation of the specific heat capacity of water-Cu nanofluids. *Int. Nano Lett.* **2013**, *3*, 58. [\[CrossRef\]](#)
68. Sann, E.E.; Pan, Y.; Gao, Z.; Zhan, S.; Xia, F.J. Highly hydrophobic ZIF-8 particles and application for oil-water separation. *Sep. Purif. Technol.* **2018**, *206*, 186–191. [\[CrossRef\]](#)
69. Yuan, J.; Li, Q.; Shen, J.; Huang, K.; Liu, G.; Zhao, J.; Duan, J.; Jin, W. Hydrophobic-functionalized ZIF-8 nanoparticles incorporated PDMS membranes for high-selective separation of propane/nitrogen. *Asia-Pac. J. Chem. Eng.* **2017**, *12*, 110–120. [\[CrossRef\]](#)
70. Zhang, K.; Lively, R.P.; Zhang, C.; Chance, R.R.; Koros, W.J.; Sholl, D.S.; Nair, S. Exploring the framework hydrophobicity and flexibility of ZIF-8: From biofuel recovery to hydrocarbon separations. *J. Phys. Chem. Lett.* **2013**, *4*, 3618–3622. [\[CrossRef\]](#)
71. Grosu, Y.; Renaudin, G.; Eroshenko, V.; Nedelec, J.-M.; Grolier, J.-P. Synergetic effect of temperature and pressure on energetic and structural characteristics of {ZIF-8+ water} molecular spring. *Nanoscale* **2015**, *7*, 8803–8810. [\[CrossRef\]](#)
72. Cheng, X.; Jiang, Z.; Cheng, X.; Yang, H.; Tang, L.; Liu, G.; Wang, M.; Wu, H.; Pan, F.; Cao, X. Water-selective permeation in hybrid membrane incorporating multi-functional hollow ZIF-8 nanospheres. *J. Membr. Sci.* **2018**, *555*, 146–156. [\[CrossRef\]](#)
73. Deng, Y.; Dai, M.; Wu, Y.; Ali, I.; Zhao, J.; Li, S.; Peng, C. High-efficient novel super-wetting HKUST-1 membrane for oil-water separation: Development, characterization and performance. *J. Clean. Prod.* **2022**, *333*, 130109. [\[CrossRef\]](#)

74. Bradshaw, D.; Garai, A.; Huo, J. Metal–organic framework growth at functional interfaces: Thin films and composites for diverse applications. *Chem. Soc. Rev.* **2012**, *41*, 2344–2381. [[CrossRef](#)]
75. Morris, R.E. Grown into shape. *Nat. Chem.* **2011**, *3*, 347–348. [[CrossRef](#)]
76. Devaux, A.; Popović, Z.; Bossart, O.; De Cola, L.; Kunzmann, A.; Calzaferri, G. Solubilisation of dye-loaded zeolite L nanocrystals. *Microporous Mesoporous Mater.* **2006**, *90*, 69–72. [[CrossRef](#)]
77. Zhao, X.; Yuan, Y.; Li, P.; Song, Z.; Ma, C.; Pan, D.; Wu, S.; Ding, T.; Guo, Z.; Wang, N. A polyether amine modified metal organic framework enhanced the CO<sub>2</sub> adsorption capacity of room temperature porous liquids. *Chem. Commun.* **2019**, *55*, 13179–13182. [[CrossRef](#)]
78. Park, K.S.; Ni, Z.; Côté, A.P.; Choi, J.Y.; Huang, R.; Uribe-Romo, F.J.; Chae, H.K.; O’Keeffe, M.; Yaghi, O.M. Exceptional chemical and thermal stability of zeolitic imidazolate frameworks. *Proc. Natl. Acad. Sci. USA* **2006**, *103*, 10186–10191. [[CrossRef](#)]
79. Giri, N.; Davidson, C.E.; Melaugh, G.; Del Pópolo, M.G.; Jones, J.T.; Hasell, T.; Cooper, A.I.; Horton, P.N.; Hursthouse, M.B.; James, S.L. Alkylated organic cages: From porous crystals to neat liquids. *Chem. Sci.* **2012**, *3*, 2153–2157. [[CrossRef](#)]
80. Chen, W.; Guo, X.; Zou, E.; Luo, M.; Chen, M.; Yang, M.; Li, H.; Jia, C.; Deng, C.; Sun, C. A continuous and high-efficiency process to separate coal bed methane with porous ZIF-8 slurry: Experimental study and mathematical modelling. *Green Energy Environ.* **2020**, *5*, 347–363. [[CrossRef](#)]
81. Yang, M.; Wang, H.; Zuo, J.Y.; Deng, C.; Liu, B.; Chai, L.; Li, K.; Xiao, H.; Xiao, P.; Wang, X. Efficient separation of butane isomers via ZIF-8 slurry on laboratory-and pilot-scale. *Nat. Commun.* **2022**, *13*, 4792. [[CrossRef](#)]
82. Mehio, N.; Dai, S.; Jiang, D.-E. Quantum Mechanical Basis for Kinetic Diameters of Small Gaseous Molecules. *J. Phys. Chem. A.* **2014**, *118*, 1150–1154. [[CrossRef](#)]
83. Vagt, U.; Emmanuel, C. Acid scavenger prevents sticky problem. *Chem. Process* **2006**, *69*, 45.
84. Agarwal, R.; Journey, P.; Raythatha, M.; Singh, V.; Sreenivasan, S.V.; Shi, L.; Roy, K. Effect of shape, size, and aspect ratio on nanoparticle penetration and distribution inside solid tissues using 3D spheroid models. *Adv. Healthc. Mater.* **2015**, *4*, 2269–2280. [[CrossRef](#)]
85. Tsalaporta, E.; MacElroy, J.D. A comparative study of the physical and chemical properties of pelletized HKUST-1, ZIF-8, ZIF-67 and UiO-66 powders. *Heliyon* **2020**, *6*, e04883. [[CrossRef](#)]

**Disclaimer/Publisher’s Note:** The statements, opinions and data contained in all publications are solely those of the individual author(s) and contributor(s) and not of MDPI and/or the editor(s). MDPI and/or the editor(s) disclaim responsibility for any injury to people or property resulting from any ideas, methods, instructions or products referred to in the content.